Structure and Phase Stability of Binary Zintl-Phase Compounds: Lithium – Group 13 Intermetallics and Metal-Doped Group 14 Clathrate Compounds

Alyssa Ker,[b] Evgeny Todorov,[c, d] Roger Rousseau,*[a] Kentaro Uehara,[b] François-Xavier Lannuzel,[b] and John S. Tse[b]

Abstract: The structure/bonding relationship in a series of intermetallic phases of Li with Al, Ga, and In was investigated by density functional theory and complemented by a model based on tight-binding theory and the method of moments. The combination of these two approaches provides a simple scheme which allows for both a comprehensive understanding of structural trends and the ability to predict low-energy structures for a given composition. This analysis gives a straightforward picture of phase stability in terms of local geometric features such as triangular, square, and hexagonal arrangements of atoms. The approach was extended to examine the structural properties of metal-doped clathrate compounds of C, Si, Ge, and Sn. Clathrate-type phases based on the frameworks Si_{172}, Ge_{172}, Si_{40}, and Ge_{40} are not only likely to be energetically favorable but may also exhibit high thermoelectric efficiency.

Keywords: density functional calculations · inclusion compounds · intermetallic phases · solid-state structures · zintl phases

Introduction

Understanding the structure and bonding of intermetallic phases poses a unique challenge to theory. First-principles calculations can be used to obtain an accurate description of the structure and physical properties of a material, such as elastic constants and thermal power. However, often the complexity of these simulations does not readily allow for the identification of the underlying physical principles which govern why the complex structures of metals and alloys are formed. On the other hand, the alloy designer or solid-state chemist can still make intermetallic phases and understand their structure and properties of by using simple models such as the Zintl – Klemm concept and Miedema's rules.[1, 2] A major achievement was the development of reliable structure maps[1, 2] that predict which phases can be formed by combining different elements. As with other models, these maps are classifications of structures by parameters such as electronegativity and number of valence electrons and are empirically derived. Thus, the answer to the fundamental question of why intermetallic phases form with a particular structure and stoichiometry is still elusive.

A step towards understanding phase stability, and ultimately predicting which phase may be obtained for a given stoichiometry, is a qualitative understanding of the structure of phase diagrams. Ideally, if we could draw a direct relationship between such concepts as electronegativity and valence electron concentration to explain why phases form in a given structure type (ST), we could then rationally design solids. From the point of view of theory, this type of paradigm would be useful in materials science to complement computationally intense first-principles studies. At present, methods based on density functional theory (DFT)[3] can now discriminate the total energies of different phases to within fractions of an electron volt. Yet, to indiscriminately search though a host of possible phases with DFT methods can place extreme demands on resources and time. Therefore, what is required is an approach to qualitatively screen structures, either by fast, low-level calculations or, more desirably, simple rules of thumb.

Here we provide such a qualitative approach based on a simple tight-binding model and analysis of the relationship between structure and phase stability by the method of moments.[1, 2, 4–8] This theory differs from traditional methods of solid-state band theory in that the analysis is performed in

[a] Dr. R. Rousseau
Lehrstuhl für Theoretische Chemie
Ruhr-Universität Bochum, 44780 Bochum (Germany)
Fax: (+49)234 321 4045
E-mail: roger.rousseau@theochem.ruhr-uni-bochum.de

[b] A. Ker, Dr. K. Uehara, Dr. F.-X. Lannuzel, Dr. J. S. Tse
Steacie Institute for Molecular Science
National Research Council of Canada
100 Sussex Drive, Ottawa, ON, K1A 0R6 (Canada)

[c] Dr. E. Todorov
Department of Chemistry and Chemical Biology
Baker Laboratory, Cornell University
Ithaca, New York, 14853-1301 (USA)

[d] Dr. E. Todorov
Current address: UOP LLC
50 E. Algonquin Road, Des Plaines, IL 60017 (USA)

  0947-6539/02/0812-2787 $ 20.00+.50/0

real space by using the direct link between phase stability and the moments, $\mu = \int E^n \rho(E) \mathrm{d}E = Tr(H^n)$ ($n = 0, 1, 2\ldots$), of the electronic density of states (DOS) $\rho(E)$. Within a tight-binding description of electronic structure, the nth moment is related to the number of closed paths of order n and hence intimately connected to local structural features. Hence, these are the perfect parameters by which to relate the crystal structure topology to the total electronic energy of the system. For example, μ_2 is related to the coordination number, μ_3 to the number of triangular arrangements of atoms, μ_4 is connected to squares and bond-angle effects, and μ_5 and μ_6, among other things, reflect the contribution of pentagons and hexagons, respectively.[2, 5–8] Previous work using this approach focused on the relationship between moments analysis and traditional electron counting rules[7, 8] to provide a link with traditional bonding concepts. These insights into the energy/structure relationship form the key to bridging the gap between the simple models and the full quantum mechanical first-principles methods.

Here we demonstrate how a relatively simple tight-binding scheme can be used to understand the structure of phase diagrams of Zintl-type compounds. In particular, we model the zero-Kelvin electronic energy stability that would be obtained from an ab initio calculation that does not include finite temperature effects for either electrons or nuclei. We also show how this can be exploited as a practical tool to complement first-principles studies of novel materials. Some of these results have been published in prior short communications,[9–12] whereas the objective of this work is to provide a more comprehensive and detailed discussion. Previous work on moments methods and Zintl-phase structures[13–16] focused upon fixed stoichiometries, in contrast to the approach here, where we examine the role of variable stoichiometry, as is necessary to understand phase diagrams.

In the next section, a detailed discussion of the simulation techniques is presented. This section may be skipped by the reader less interested in this aspect of the work without loss of continuity. We then provide a detailed investigation of phase stability for intermetallics and alloys of Li and the Group 13 elements Al, Ga, and In. A database of state-of-the-art calculations for Li – Al alloys[17–21] demonstrates that current electron structure theory is sufficiently accurate to reproduce the phase stability, yet a simple picture of the underlying physics is still lacking. Here we examine bonding in real space of these compounds and show how a qualitative model allows us to understand the low-temperature phase diagram. The simple rules derived from this analysis are then used to make educated predictions of alternative low-energy Li – Al phases, which are verified by DFT simulation. Finally, these concepts are extended to understanding the phase stability of Group 14 clathrate structures.[22–29] Compounds of this type have received enormous attention, both theoretical[31–39] and experimental, due to their interesting electrical transport properties, most notably superconductivity[30] and high thermoelectric efficiency.[9, 40–45] Within this section we present predictions of novel clathrate-type structures which are not only energetically compatible with known phases but may also be suitable for application as highly efficient thermoelectric materials.

Computational Methods

Tight-binding simulations and moments expansions: We employ the second-moment-scaled Hückel tight-binding model,[46, 47] which has met with great success in rationalizing structural trends in solid-state phases.[2, 7, 8] The method is described in several reviews[7, 8] and compared with ab initio electronic structure theory,[48, 49] so the relative performance and weaknesses of the method are well documented. Therefore, this approach need not be expanded upon in detail here, except for the specific cases where methodological changes are introduced.

The structures used for tight-binding simulations were obtained from fully optimized geometries, including cell parameters, at the DFT level. For the tight-binding analysis, each main group atom is modeled by including the valence s and p atomic orbitals. The electropositive alkali and alkaline earth metal atoms are assumed to transfer all valence electrons to the main group atoms, and are thus considered to act simply as point charges. We verified the ionic nature of these interactions in the Na – Si and Li – Al phases at the DFT level of theory in a previous communication.[9, 10] Here we neglect the ionic contribution to the total electronic energy which was included in previous studies,[48–50] and only consider the covalent or band-structure energy. This simplifies our computational scheme by removing the need to include up to four extra parameters (and their dependence upon electron concentration) for an ionic term. This approximation is most valid when the relative charges on the ions are low and the number of covalent bonds between main group atoms is high, that is, large bonding and small ionic energies. Note that in cases such as lanthanide compounds of Group 16 elements,[50] in which there are few covalent bonds and large formal charges, a predomint role of the covalent energies in ultimately determining the final structure was observed. Only interactions between main group atoms whose distance falls within the first peak of the radial distribution function are included in the tight-binding analysis, and all other Hamiltonian matrix elements are set to zero. This simplifies the model and avoids the tendency of Hückel methods to overestimate interactions with second-nearest neighbors. A mesh of at least 1000 $\boldsymbol{k}$ points over the symmetry-inequivalent portion of the Brillouin Zone (BZ) was used to insure convergence of moments and energies.

The methodology adopted here differs from previous implementations in two respects. First, the μ_2 of the various structures are scaled by a simple renormalization of the eigenvalue spectrum, as opposed to iteratively rescaling the size of the system such that all phases have identical second moments. The structural energy difference theorem[47] (on which the second-moment scaling hypothesis is based) applies only for small variations in the system size, for which the width but not the shape of the DOS is affected. Thus, this further approximation is also appropriate. This has the advantage of reducing the computational effort to one-eighth to one-tenth of that of the former approach. We validated this assumption by repeating the simulation of the Li – Al phase diagram and found that the two approaches yield energy difference curves which are qualitatively identical in that the electron counts over which phases are stable differ by at most 0.02 e per atom. Thus, the approach is reduced to performing a single Hückel calculation for each structure to obtain eigenvalues, which are then manipulated to obtain DOS and moments.

A second modification to previous studies is in the way in which we obtained the Hückel parameters for our simulations. All orbital exponents are obtained directly from fitting the radial wavefunction obtained from scalar-relativistic LDA-DFT atomic calculations to single-exponent Slater functions. We do not necessarily use the ground-state atomic configurations, but employ that used to generate transferable pseudopotentials (see ref.[51] for a description of the configurations used for s, p, and d states of each atom). The energy separation between the ionization values of the s and p electrons, denoted ΔH_{ii}, is also obtained from the atomic calculations. This leaves only one parameter, namely, the absolute energy level of the atomic p orbital. For this, we take as an initial value the ionization energy from a well-established parameter set[52] and allow it to vary to obtain the best agreement for the trend of structure type versus number of valence electrons for phase boundaries of the Li – Group 13 element phase diagram. The values of the parameters obtained form the above procedure for Group 14 elements are given in Table 1. The results of these tight-binding simulations are qualitatively insensitive to the parameters used and to the small variation between parameters of elements of Groups 13 and 14.

  0947-6539/02/0812-2788 $ 20.00+.50/0 *Chem. Eur. J.* **2002**, *8*, No. 12

Table 1. Parameters used in tight-binding simulations (see text for details).

Element	n	ζ_s	H_{ss}	ζ_p	H_{pp}
C	2	1.625	−21.40	1.625	−11.40
Al/Si	3	1.70	−15.50	1.38	−7.30
Ga/Ge	4	2.31	−13.30	1.60	−7.30
In/Sn	5	2.60	−12.60	1.90	−6.19

In general, the ordering of which phases are stable with respect to increasing electron count is not altered by variations of this parameter over several electron volts, but the electron count at which a given phase becomes stable can change by as much as 0.5 e per atom. Hence, we restricted ourselves to only one sp block atom for each row of the periodic table, and this leads to greater simplification of the model. The parameters accurately account for several key trends as one goes down a column of the periodic table. First, the ionization potential decreases from C to Sn. Second, both s and p orbital exponents become more contracted, and the relative contraction of the s outweighs those of the p. Finally, our parameterization for first row sp-bonded elements leads to values which are essentially identical to the traditional parameters for C, and thus we opted to use these.

The results of the tight-binding analysis were examined within the method of moments[2, 5, 6] which was adapted to our purpose by the following prescription. First, an accurate representation of the DOS $\rho(E)$ and its moments $\mu_i = \int E^i \rho(E) \mathrm{d}E$ is obtained from our tight-binding calculation. The eigenvalues are then renormalized such that $\mu_0 = 1$, $\mu_1 = 0$, and $\mu_2 = \mu_2(\text{diamond})$, where $\mu_2(\text{diamond})$ is the second moment for the diamond structure. Note that the choice of μ_2 does not alter the phase ordering due to renormalization of the eigenvalue employed here. The results of the tight-binding calculation can then be examined in terms of the contributions of the specific moments by the following procedure. The DOS can be constructed from its moments via a continued fraction [Eq. (1)], where IM indicates the imaginary part, f is a function which terminates the fraction (see below), and the coefficients a_n and b_n are obtained from the moments μ_i via determinants A_n and B_n [Eqs. (2) and (3)] and the recursion formula [Eq. (4)], where $a_0 = 1$, $a_1 = A_1$, $b_0 = 0$ (by definition).

$$\rho(E) = \frac{1}{\pi} IM \left\{ \frac{a_0}{E + b_0 - \cfrac{a_1}{E+b_1 - \cfrac{a_2}{E+b_2 - f}}} \right\} \tag{1}$$

$$A_n = \begin{vmatrix} \mu_0 & \mu_1 & \cdots & \mu_{n-1} & \mu_n \\ \mu_1 & \mu_2 & \cdots & \mu_n & \mu_{n+1} \\ \vdots & \vdots & \cdots & \vdots & \vdots \\ \mu_n & \mu_{n+1} & \cdots & \mu_{2n-1} & \mu_{2n} \end{vmatrix} \tag{2}$$

$$B_n = \begin{vmatrix} \mu_0 & \mu_1 & \cdots & \mu_{n-1} & \mu_{n+1} \\ \mu_1 & \mu_2 & \cdots & \mu_n & \mu_{n+2} \\ \vdots & \vdots & \cdots & \vdots & \vdots \\ \mu_n & \mu_{n+1} & \cdots & \mu_{2n-1} & \mu_{2n+1} \end{vmatrix} \tag{3}$$

$$a_n = \frac{A_{n-2}A_n}{A_{n-1}^2}, \; b_n = \frac{B_n}{A_n} - \frac{B_{n-1}}{A_{n-1}} \tag{4}$$

Successive terms in the continued fraction of Equation (1) account for the contribution of even increasing moments and allow us to build up the DOS. The above algorithm for obtaining the coefficients in Equations (2)–(4) differs from the formulas presented previously in ref. [5, 6] for the calculation of b_n in having greater numerical stability.

Termination of the continued fraction to allow for accurate evaluation has been the subject of several studies.[53, 54] We adopt the simplest of these schemes by noting that for most systems a_n and b_n approach limiting values a_{final} and b_{final}, thus providing the relation of Equation (5), which can be solved to give Equation (6).

$$f = \frac{a_{final}}{E + b_{final} - f} \tag{5}$$

$$f = \frac{E + b_{final} + \sqrt{(E + b_{final})^2 - 4a_{final}}}{2} \tag{6}$$

This provides the simple solution $E_u = -b_{\text{final}} + 2\sqrt{a_{\text{final}}}$ and $E_l = -b_{\text{final}} - 2\sqrt{a_{\text{final}}}$ where E_u and E_l are the highest and lowest orbital energies. Equation (6) can be used to truncate Equation (1) at any given value of a_n or b_n, and this effectively eliminates the information contained in the higher order moments. This in principle allows us to examine how the various moments, and hence how the local structural motifs, affect the total electronic energy and ultimately the phase stability.

DFT simulations and properties derived from the Fermi surface: To validate the theoretical predictions of the simpler tight-binding model and to obtain predicted properties of these phases, we performed calculations based on DFT.[3] In particular, the core electrons were modeled by an ultrasoft pseudopotential[55] including only the outermost s and p electrons in the valence shell. These electrons were expanded in a basis set of plane waves with a cutoff energy of 1.5 times that of the recommended value for convergence to high accuracy. A Monkhorst–Pack[56] $10 \times 10 \times 10$ mesh of $\boldsymbol{k}$ points was used for BZ integration to insure convergence of the total energy to within 0.01 eV per atom, with the exception of X_{136} and X_{172} (X = C, Si, Ge, Sn). For these phases the large unit cells allowed smaller $\boldsymbol{k}$ meshes of $6 \times 6 \times 6$ and $4 \times 4 \times 6$ (X_{136} and X_{172}, respectively) to give the same level of convergence. Results were obtained within the local density (LDA) and generalized gradient (GGA)[57] approximations for the Li–Al system. As a gauge for the accuracy of our calculations relevant structural parameters are compiled in Table 2 for the Li–Al system. As expected, both LDA and GGA provide accurate lattice constants and bond lengths within about 2% of those observed experimentally. The values provided by LDA are characteristically lower but in agreement with those of previous studies.[17–21] Both functionals reproduce the trend of decreasing Al–Al bond length with increasing Li concentration. Only LDA calculations were employed for the Group 14 clathrate compounds. The validity of the rigid-band approximation has been discussed at length elsewhere,[9] and analogous calculations performed on some of the current structures

Table 2. Structural parameters for Li–Al binary phases.

Phase	Structure type	Valence electrons	No. of Al–Al bonds	Lattice constants [Å], exptl (LDA, GGA)[a]	Al-Al [Å], exptl (LDA, GGA)[b]
Al	Cu (fcc)	3	12	a = 4.05 (3.99, 4.04)	2.86 (2.82, 286)
$LiAl_3$	Au_3Cu	3.33	8	a = 4.01 (3.96, 4.01)	2.83 (2.79, 2.83)
LiAl	NaTl	4	4	a = 6.36 (6.23, 6.31)	2.76 (2.70, 2.73)
Li_3Al_2	Bi_2Te_3	4.5	3	a = 4.50 (4.37, 4.43) c = 14.25 (13.75, 13.92)	2.74 (2.67, 2.71)
Li_9Al_4	Li_9Al_4	5.25	2	a = 19.15 (18.45, 18.69) b = 5.42 (5.23, 5.32) c = 4.50 (4.38, 4.44)	2.64 (2.65, 2.68)
Li_2Al_3	Ga_2Ti_3	3.67	6.67	a = (6.21, 6.30) c = (3.97, 4.03)	(2.79, 2.83)[b]
Li_5Al_4	Li_5Ga_4	4.25	5.50	a = (4.37, 4.42) c = (8.19, 8.23)	(2.69, 2.71)[b]

[a] Calculated values. [b] Average.

yielded similar findings. DFT calculations were performed with the Vienna Ab Initio Software Package (VASP).[58–60]

The thermoelectric figure of merit (ZT) of a material is governed by Equation (7), where S is the temperature-dependent Seebeck coefficient,[61] σ is the electrical conductivity, and κ is the thermal conductivity. For crystals $S(T)$ can be calculated, within the approximation of constant relaxation time τ, from a knowledge of the DOS ρ(E), the velocity of the electrons at the Fermi level v, and the Fermi distribution [Eq. (8)],[61] where L^x is given by Equation (9), such that [Eq. (10)], and for metals at low temperature [Eq. (11)].

$$ZT = TS^2\frac{\sigma}{\kappa} \tag{7}$$

$$S(T) = \frac{L^1}{eTL^0} \tag{8}$$

$$L^x = \tau \int dE(E - E_{Fermi})^x v^2(E)\rho(E)\left[-\frac{\partial f(E)}{\partial E}\right] \tag{9}$$

$$L^0 = \frac{e^2}{3\hbar}\sigma \tag{10}$$

$$L^1 = -\frac{\pi^2}{3e}k^2T\left[\frac{\partial\sigma(E)}{\partial E}\right]_{E=E_{Fermi}} \tag{11}$$

Thus, the Seebeck coefficient is related to the reciprocal electrical conductivity and the first derivative of the conductivity near the Fermi energy. Here it is assumed that each partially occupied band behaves independently. In general, S is largest in systems having partially occupied bands with low v and hence only weak dispersion. Thus, structures with flat bands at and around the Fermi level are the best candidates to obtain large values of S.

Transport properties of the hypothetical X_{40} clathrate phases (see below) were modeled by a similar prescription to our previous work on Na-doped Si clathrate phases.[9, 62] BZ integration was carried out by using a modified Shankland–Koelling–Wood band-interpolation scheme.[63, 64] First, we calculated eigenvalues on relatively coarse three-dimensional $\boldsymbol{k}$ point grids. Second, these eigenvalues are interpolated on the basis of lattice star function expansion to give the eigenvalues on dense $\boldsymbol{k}$ point grids. For each compound, 1000 and 10000 $\boldsymbol{k}$ points in the first BZ are used as coarse and dense $\boldsymbol{k}$ point grids.

The reliability of the ultrasoft pseudopotential calculation was examined by comparing the results with full-potential linearized augmented plane wave (FLAPW) code.[65] The reasonable agreement between the two methods confirms the reliability of our data.

Results and Discussion

Phase diagrams of Li–Group 13 intermetallics: *Phase ordering with increasing Li concentration*: Lithium was chosen as alkali metal due to its relatively small ionic radius, which thus lessens the effects of the size of alkali metal cation and may lead to structures with discrete clusters.[66] This allows us to examine the energy dependence of infinite networks. Here we assess the validity of using a moments scheme to account for boundaries on the phase diagram of a variable ratio of Li to Group 13 element.

The low-temperature Li–Al phase diagram is fairly simple[67] and comprises five known phases: Al (fcc), LiAl (NaTl ST), Li_3Al_2 (Bi_2Te_3 ST), Li_9Al_4 (Li_9Al_4 ST), and elemental Li (bcc at 300 K). These structures are shown in Figure 1 in order of increasing Li to Group 13 atomic ratio. We also include the metastable phase $LiAl_3$ ($AuCu_3$ ST) in this discussion, which on the basis of electronic energy (as opposed to free energy) is energetically compatible with the stable phases. Similar to Li–Al the phase diagrams of Li–In and Li–Ga also contain the 1:1 phase in the NaTl ST and the 3:2 Bi_2Te_3 ST (see Figure 1). However, both In and Ga form an additional 5:4 phase with the Li_5Ga_4 ST, as well as a 2:1 phase of the Li_2Ga ST, in contrast to the 9:4 stoichiometry of Li–Al. Most interesting is the differences in the structures found at low Li concentration. Elemental Al has an fcc structure, whereas Ga has a unique seven-coordinate structure (see ref. [68] for detailed analysis), and In has a tetragonally distorted fcc phase. In addition, Li–Ga exhibits a phase with stoichiometry 3:14 (Li_3Ga_{14} ST).

Consider the relationship between the valence electron concentration and the structural motifs exhibited by the Al sublattices in the series of Li–Al phases. The first member, elemental Al, has three valence electrons per atom (3 e atom^{-1}) and a total of twelve Al–Al contacts. $LiAl_3$ has 4.33 e atom^{-1}, LiAl 4 e atom^{-1}, Li_3Al_2 4.5 e atom^{-1}, and for Li_9Al_4 5.25 e atom^{-1}. The trend in the structural changes and the band filling bears a striking similarity to the well-known trends for solid-state elemental phases, as exemplified by the sp-valent elements in the third row of the periodic table.[68] In this case, the Cu (1 e atom^{-1}) and Zn (2 e atom^{-1}) structures are closest packed with twelve nearest neighbors, while Ga (3 e atom^{-1}) has a coordination number of seven, Ge (4 e atom^{-1}) is four-coordinate and exists in the diamond structure, As (5 e atom^{-1}) forms sheets (similar to the aluminum layers of Li_3Al_2) with a coordination number of three, and Se (6 e atom^{-1}) exists in two-coordinate chains. This trend, which can be rationalized by using the language of moments,[68] strongly indicates that an analogous explanation underlies the phase stability in Li–Al binary systems.

This is validated by the moments analysis of the DOS. Figure 2a compares the total energy differences, obtained from tight-binding calculations, between the various Al sublattices to that of Li–Al as a function of the number of valence electrons. The convention of these curves is that the structure with the highest energy for a given electron concentration is most stable at that electron count. The total-energy curves can be reconstructed by expanding the DOS in terms of contributions from the various moments by a continued fraction expansion, which can be truncated at a given moment. This allows the determination of the relevant moment, and hence the geometrical features, that control the phase stability (see Figure 2b,c). The relationship of the shape of these curves to the moments has been fully developed elsewhere. In general, the number of nodes (including the two end points) in these curves is equal to the moment which is most responsible for the energy difference between two structures.

This modest calculation provides values for the phase boundaries which are in good agreement with experiment. Figure 2a shows that LiAl is stable at 3.1–4.4 e atom^{-1}, followed by Li_3Al_2 between 4.4 e atom^{-1} and 5.6 e atom^{-1}, and Li_9Al_4 becomes stable for electron counts greater than or equal to 5.6 e atom^{-1} (slightly higher then the experimental 5.25 e atom^{-1}). Elemental Al is the most stable structure at

  0947-6539/02/0812-2790 $ 20.00+.50/0 *Chem. Eur. J.* **2002**, *8*, No. 12

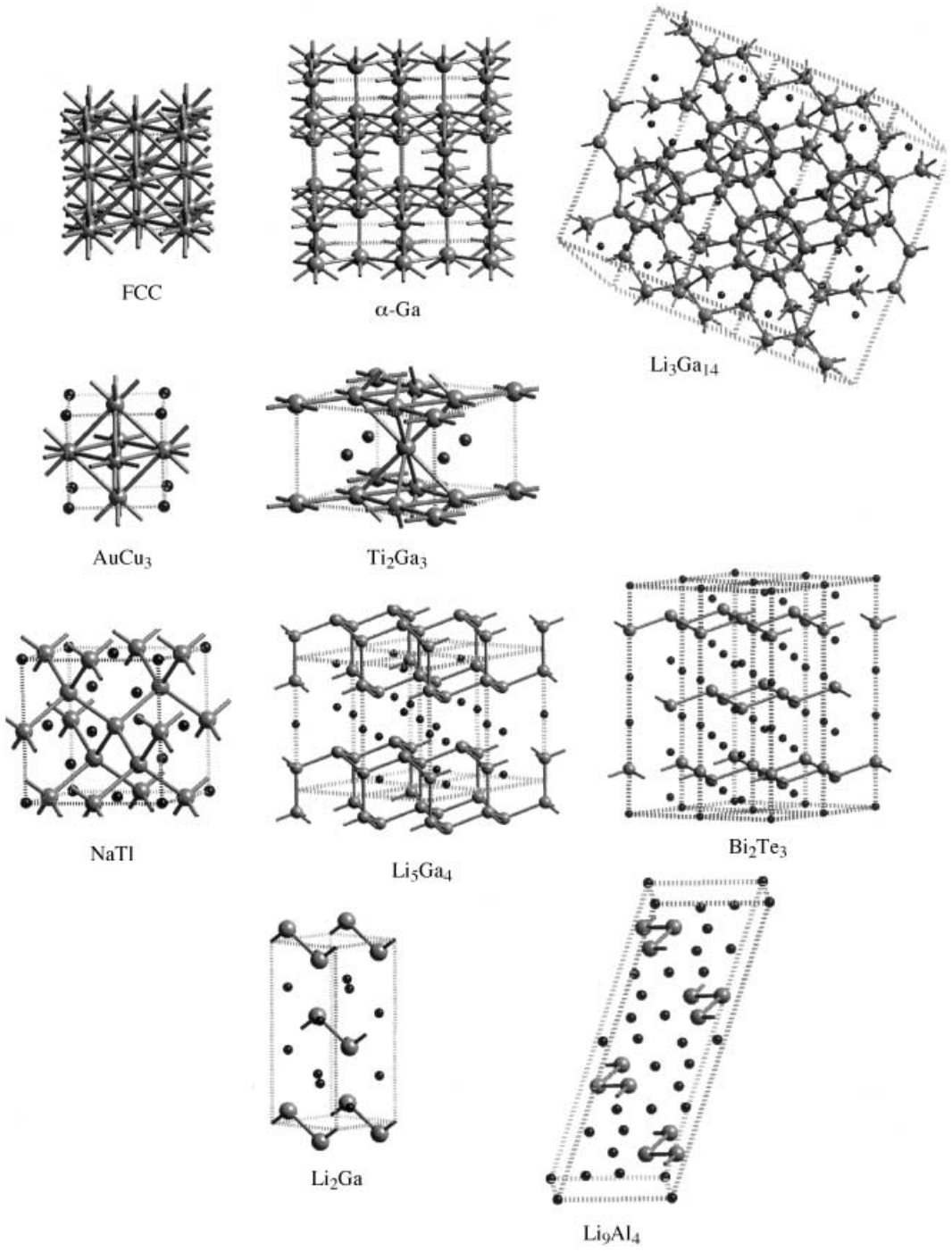

Figure 1. Structures of Li – Group 13 compounds. fcc (Al and In). α-Ga, Li_3Ga_{14}, $AuCu_3$ (metastable $LiAl_3$), Ti_2Ga_3 (hypothetical Li_2Al_3), NaTl (LiAl, LiGa, and LiIn), Li_5Ga_4 (Li_5Ga_4 and Li_5In_4), Bi_2Te_3 (Li_3Al_2 Li_3Ga_2, and Li_3In_2), Li_2Ga (Li_2Ga and Li_2In), and Li_9Al_4. Group 13 atoms are represented by gray spheres, and Li atoms by small black spheres. In accordance with the Zintl description, only bonds between Group 13 atoms are drawn.

low electron count ($3\ e\ atom^{-1}$), and the energy difference curve has three nodes, which is indicative of a third-moment effect. This is caused by the the large number of triangular faces of the polyhedra in an fcc structure. This observation is corroborated by the fact that the reconstructed energy-difference curve converges fully with the exact result in terms of amplitude and crossover point by considering only up to the third moment. The stability of the chains in Li_9Al_4 relative to LiAl at high electron counts can be traced back to the large fourth moment and its relationship to the coordination number.[8] In general, scaling μ_2 shifts coordination number into the fourth moment, which increases with decreasing coordination number due to the renormalization of the eigenvalues. The Li_3Al_2 curve is only fully converged when the sixth moment is included, even though it has four nodes. This behavior is due to the importance of the large number of six-membered rings in the LiAl structure and in the Al sheets of Li_3Al_2. These rings lead to stability at the half-filled band, but are less stable just above and below. In general, the method reproduces the approximate electron count at which

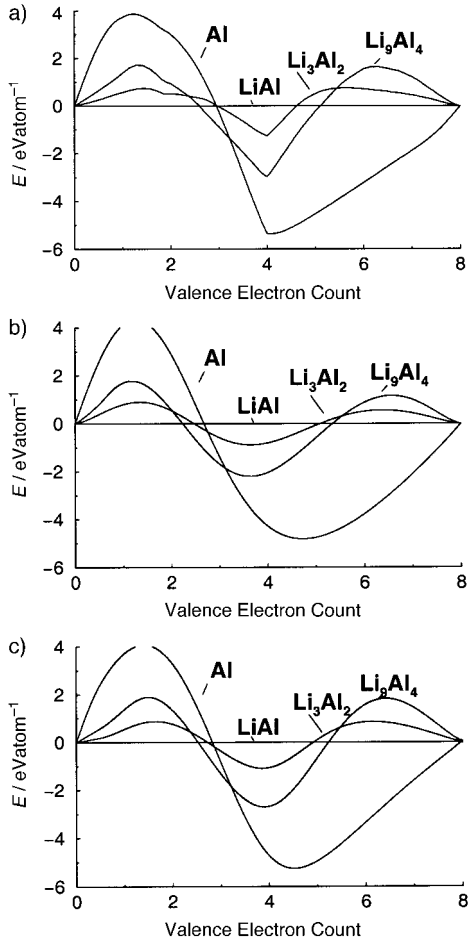

Figure 2. Energy-difference curves for the stable phases of Li – Al, obtained by comparing the total electronic energies from tight-binding calculations (a). The curves are reproduced by continued fraction expansion of the DOS with a series of moments truncated at μ_4 (b) and μ_6 (c). The convention of these plots is that the structure with the highest energy at a given fractional band filling is the most stable at that electron count.

specific structural motifs are found to be stable with maximum observed errors of 0.4 e atom^{-1}.

Similar trends are found for both the Li – Ga and Li – In phase diagrams (Figure 3). Indium is in a distorted fcc phase and dominates at lower electron counts. However, this phase is not stable at 3 e atom^{-1} for Ga, for which α-Ga is dominant over fcc Ga. Each Ga atom in α-Ga participates in six triangles, whereas a slight increase in the number electrons makes the Li_3Ga_{14} phase more stable. This is due to the lower third moment of Li_3Ga_{14}. In this phase each Ga atom is contained in an icosahedron and is involved in five triangles per atom. Above the half-filled band for both In and Ga the Li_5Ga_4 ST is observed, as well as Bi_2Te_3. In Li_5Ga_4 the most prevalent structural component is a bilayer of puckered hexagonal sheets. These same sheets also exist in the Tl sublattice of the NaTl structure, as can be readily seen by looking down the (111) crystallographic axis. One can derive the structure of Li_3Ga_2 by breaking the Ga bonds between each sheet in the (111) direction, and the bilayer of Li_5Ga_4 by performing this procedure for alternate layers only. This natural progression is expressed in the language of moments

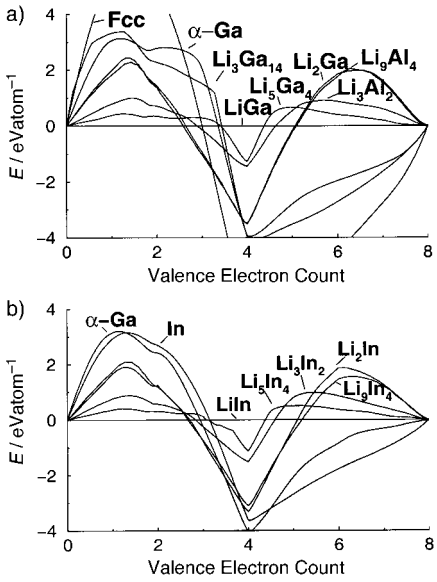

Figure 3. Energy-difference curves for the stable phases of Li – Ga (a) and Li – In (b), obtained by comparing the total electronic energies from tight-binding calculations. The convention of these plots is the same as Figure 2.

by a reduction of both coordination number (μ_4 effect) and the number of six-membered rings (μ_6 effect). Finally, both phases exhibit chain structures at an electron counts above 5.4 e atom^{-1}, which is slightly higher then the observed value of 5.0 e atom^{-1}.

The model also provides qualitative insights into trends in the phase boundaries of the different Group 13 elements. For instance, the results of Figure 3 show that for Ga the α-Ga structure is preferred over the fcc structure, but it for In it is destabilized. This is due to the different weighting of the triangular motifs in the third moment as a function of the orbital exponents. Likewise, the Li_9Al_4 ST is less stable then the Li_2Ga ST for both Ga and In as a result of a weak fourth-moment effect. This latter observation is less pronounced for Ga, for which the chains are essentially iso-energetic, and in the former case for fcc In versus α-Ga. In such cases the reliability of the method may depend on variables such as the structure used in the simulation and $\boldsymbol{k}$ space sampling.

Overall, a simple moments model accounts for the trends in bonding pattern versus electron concentration across the Li-doped Group 13 compounds. The moment analysis does more than just qualitatively account for the ordering of stable structure types; it also provides a unique insight into the local structural motifs that stabilize them. At low electron count, the preferred structural features are triangular faces. Hexagons are favored around the half-filled band, followed by squares and chains at increasing numbers of valence electrons.

Alternative structures: To illustrate the utility of this approach in designing and predicting new structures we now focus on considering phases which have not been observed experimentally. We illustrate how the structural trends can be applied to understand why alternative structures of $LiAl_3$ and LiAl which have been suggested previously[20, 21] are not the energetic ground state.

  0947-6539/02/0812-2792 $ 20.00+.50/0 *Chem. Eur. J.* **2002**, *8*, No. 12

The energy difference curve between the hypothetical BiF_3 ST and the $AuCu_3$ ST of $LiAl_3$ is shown in Figure 4a. Its shape is indicative of a third-moment effect, which is related to the fact that in BiF_3 there are too few triangles for it to be stable at

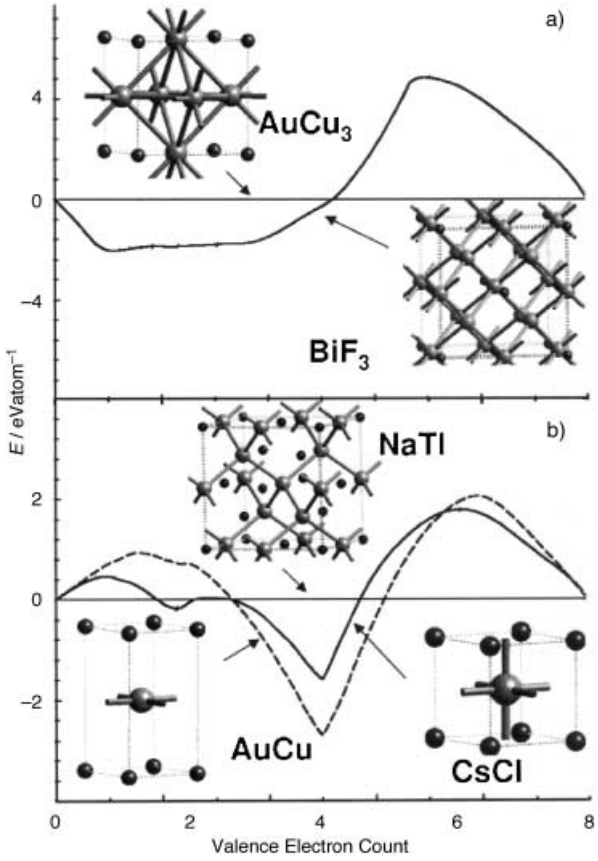

Figure 4. Energy-difference curves for alternative $LiAl_3$ and LiAl structures. The convention for these plots is the same as in Figure 2. Li is represented by small black spheres, and Al by large gray spheres.

low electron count. Similarly, if one considers LiAl in the CsCl lattice with a simple cubic Al sublattice or the AuCu ST with square sheets of Al, neither has the hexagons which are required at the half-filled band. Both of these phases have too many squares of atoms and are thus more stable at higher electron count, as illustrated by the strong fourth-moment component of the energy difference curves in Figure 4b. This then rationalizes the results of ab initio simulation[20, 21] and provides us with confidence that our approach can be used for structural prediction.

An important aspect of phase stability is the prediction of which phase can be formed at a given stoichiometry. To illustrate the power of the moments approach, we consider two hypothetical stoichiometries, Li_5Al_4 and Li_2Al_3. The former seems a likely candidate to be a stable phase when one considers the phase diagrams of Li–In and Li–Ga. This is borne out in the energy difference curves of Figure 5a, which show a small region of stability for the Al bilayer between those of LiAl and Li_3Al_2. As with Li_3Al_2, a moments decomposition of this result requires up to μ_6 for proper convergence due to the importance of both of these factors. To test this conclusion, the structure of Li_5Al_4[20, 21] was optimized

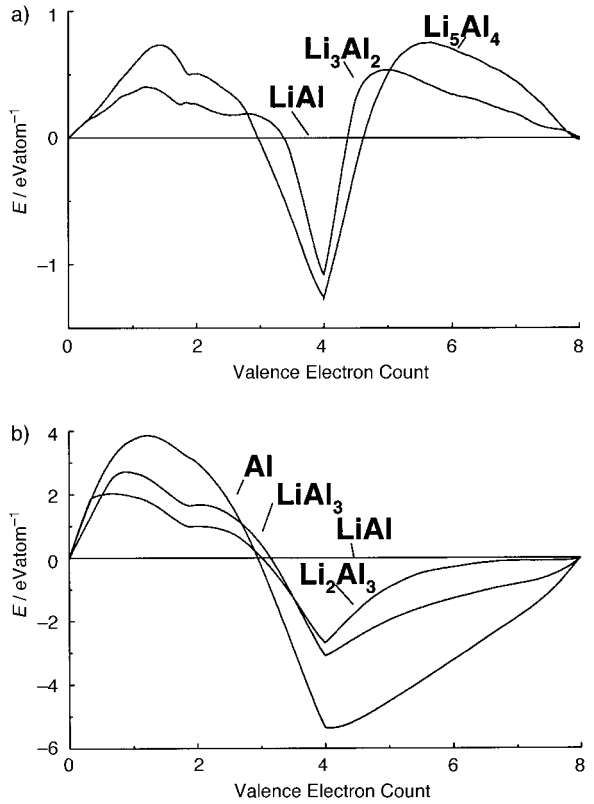

Figure 5. Energy-difference curves. a) Li_5Al_4 (Li_5Ga_4 ST) relative to LiAl and Li_3Al_2. b) Li_2Al_3 (Ti_2Ga_3 ST) and $LiAl_3$ relative to Al and LiAl. The convention for these plots is the same as in Figure 2.

at the DFT level, and its total electronic energy was compared with respect to disproportionation into LiAl and Li_3Al_2. Both LDA and GGA find that disproportionation is unfavorable by about 1–2 kcal mol^{-1}, and this suggests that on a strictly energetic criterion this phase could be stable. This criterion is not sufficient to prove this phase is stable, as one must actually consider free energy; however, this point is not the current objective. What is important is that an energetically viable structure was arrived at in a very simple and rational way based on a real-space understanding of the structure/bonding relationship.

As a second and more rigorous example, the series Al, $LiAl_3$, and Li_2Al_3 (3.67 e atom^{-1}), is considered. The analysis of structural trends as presented so far allows us to anticipate a few important features even before performing any calculations. From a comparison with the trends discussed above, we expect that the number of Al–Al bonds per atom must be between 4 and 8, intermediate between those of $LiAl_3$ and LiAl. Furthermore, the number of triangular motifs should decrease, accompanied by an increase in the number of hexagons, which are stable near the half-filled band. To test this hypothesis in an unbiased way we performed DFT calculations and geometry optimizations for Li_2Al_3 in eleven different A_2B_3 structures.[70] This search yielded the Ga_3Ti_2[69] ST (see Figure 1) as the most likely candidate, which confirms the analysis based on structural motifs. Like $LiAl_3$, this Li_2Al_3 phase may be constructed from a supercell of fcc Al by replacing some of the Al with Li atoms, and it also contains Al_6 octahedra as building blocks. The main difference is that

in $LiAl_3$ these octahedra are joined to each other at all six corners, but in Li_2Al_3 there are two inter-octahedral Al–Al bonds at four of these corners, which allows for the presence of six-membered rings and results in two eight-coordinate and four six-coordinate Al atoms. The moments analysis of $LiAl_3$ and Li_2Al_3 relative to Al and LiAl is shown in Figure 5b. Both of these phases are energetically favored relative to Al for electron counts greater than 3 e atom^{-1} due to the decrease in the number of triangles in each structure relative to the fcc structure, which is expressed as a difference in μ_3. However, both are less favorable than LiAl for valence electron counts less than 3.2 e atom^{-1}, because they have too many triangles. This finding correlates well with DFT calculations, which showed that Li_2Al_3 is unstable with respect to disproportionation into Al and LiAl by about 2 kcal mol^{-1}. Thus, again we are able to rationally pick structures which are energetically competitive with known phases.

Group 14 clathrates: Here we demonstrate how our approach can be exploited as a practical tool for studies on novel materials. We apply our analysis to understanding the phase stability of novel Group 14 clathrates and investigate their thermoelectric properties. Although there has been much theoretical work on Group 14 clathrates,[31–38] none of these studies has focused on examining the relationship between phase stability and doping level. Specifically, we sought alternatives to the experimental structures,[22–29] determined the amount of electropositive metal dopant needed to stabilize these phases, and determined whether they have desirable thermoelectric properties. Note that in these compounds resonant phonon scattering,[9, 44, 45] in which the localized vibrations of the dopant atom couple with the phonon modes of the clathrate framework, can lower the overall thermal conductivity, and this makes them desirable for practical application. This mechanism was shown to be operational in known Na–Si compounds[9] and is likely to also occur in similar species. Moreover, removal of some of the alkali metal atoms allows the doping level to be systematically altered, and the electronic component of thermal power may thus also be maximized.

We begin this discussion with a description of a series of representative cage frameworks for these clathrate phases. See Figure 6 for graphical representations, and Table 3 for a summary of the cage types and an analysis of which metal atoms fit in the cages. For each structure the average distances between the centers of the constituent polyhedra and their vertices was calculated. The van der Waals radius of the corresponding framework atom was subtracted from this value, and the remainder represents the radius of the cavity in the cage which is available for an alkali or alkaline earth metal atom. The problem is that the dopant atom can fill the accessible space or it can rattle around in it. Comparison of our analysis with the known compounds of clathrate-I shows that we can accept values of approximately 60–110% for the

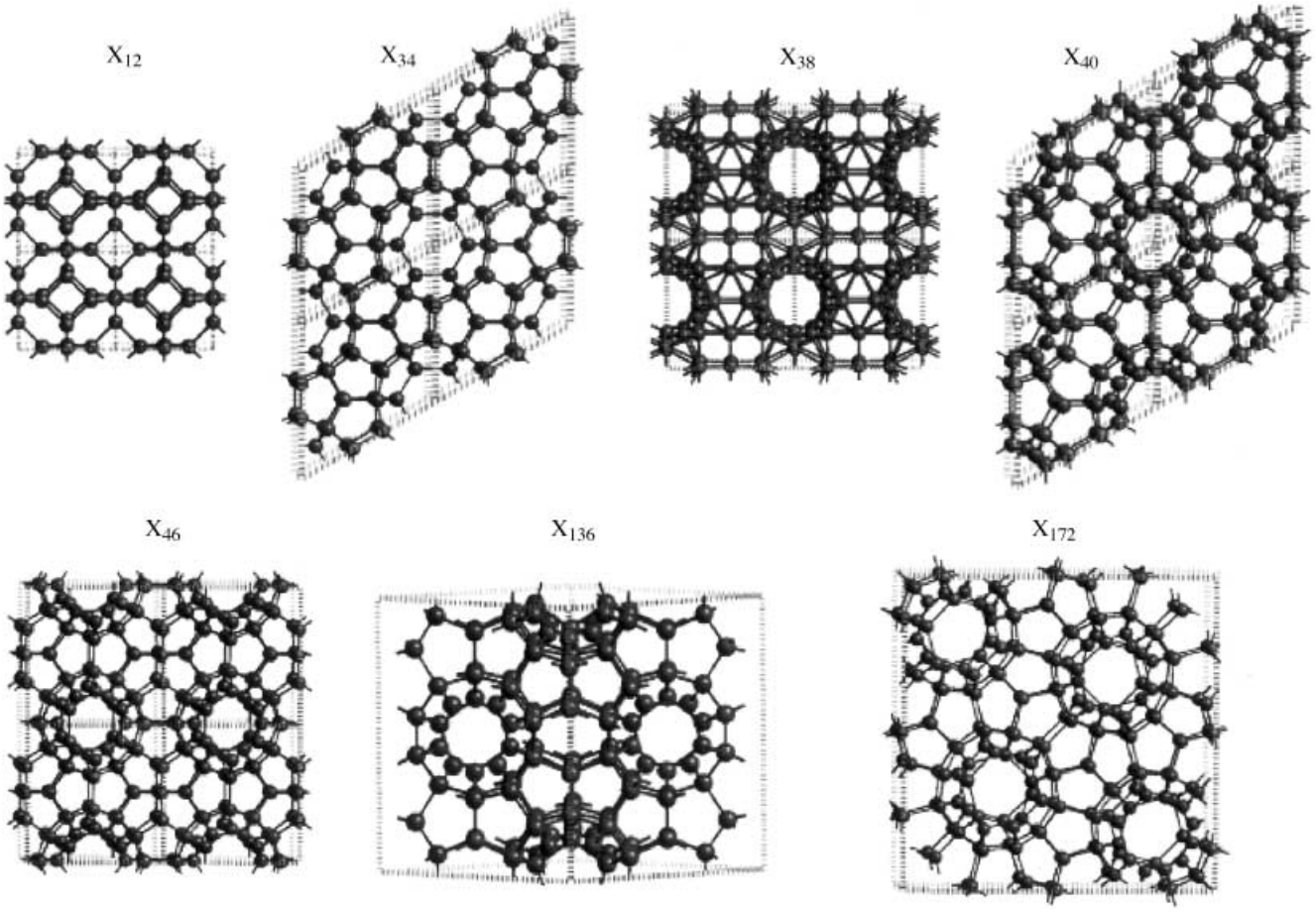

Figure 6. Representative Group 14 clathrate cage frameworks.

0947-6539/02/0812-2794 $ 20.00+.50/0 *Chem. Eur. J.* **2002**, *8*, No. 12

Table 3. Description of clathrate frameworks. For each structure we describe the cage type (for those cages which are most likely to hold guest species) and the location of the cage center. An estimate of the ions which may fit into several cages is also provided with a percentage ionic radius/cage diameter ratio. See text for details.

X_{12}		
cages:	$4^6 6^8$	at [1/2,1/2,1/2]
	ionic radii for cations per cage	
C	0.719	Li(83)/Mg(90)
Si	1.609	Rb(92)/Ba(84)
Ge	1.744	Cs(97)/Ba(77)
Sn	2.282	Cs(74)
X_{34}		
cage:	5^{12}	at [1/2,1/2,1/2]
cage:	$4^3 5^6 6^3$	at [2/3,1/3,0]
cage:	$5^{12} 6^4$	at [0,0,0]
	cationic radii per cage	
C	0.452 0.478 1.228	Be(69), Be(65), Na(77)/Ca(81)
Si	1.182 1.226 2.373	Na(80)/Ca(84)/Sr(96), Na(77)/Ca(81)/Sr(92), Cs(71)
Ge	1.278 1.327 2.520	big/too big
Sn	1.742 1.800 3.167	big/too big
X_{38}		
cage:	5^{12}	at [1/2,1/2,1/2]
cage:	$5^{12} 6^2$	at [1/4,1/2,0]
	cationic radii per cage	
C	0.722 0.556	Li(83)/Mg(90), Be(56)/Li(108)
Si	0.491 (1.001) 1.148	Mg(65)/Na(95)/Ca(99), Na(83)/Ca(86)/Sr(98)
Ge	0.668 (1.212) 1.359	Li(90)/Mg(97)/Na(78)/Ca(82)/Sr(93), Sr(83)/K(97)
Sn	1.598 1.789	Sr(71)/K(83)/Ba(84)/Rb(93), K(74)/Ba(75)/Rb(83)/Cs(94)
X_{40}		
cage:	5^{12}	at [1/2,1/2,0]
cage:	$5^{12} 6^2$	at [0,0,1/4]
cage:	$5^{12} 6^3$	at [1/3,2/3,1/2]
	cationic radii per cage	
C	0.432 0.699 0.798	Be(72), Li(86)/Mg(93), Li(75)/Mg(81)
Si	1.160 1.543 1.691	Na(82)/Ca(85)/Sr(97), K(86)/Ba(87)/Rb(96), K(79)/Ba(80)/Rb(88)/Cs(100)
Ge	1.254 1.657 1.813	Na(76)/Ca(79)/Sr(90), K(80)/Ba(81)/Rb(89), K(73)/Ba(74)/Rb(82)/Cs(93)
Sn	1.716 2.144 2.348	K(78)/Ba(79)/Rb(86)/Cs(98), K(62)/Ba(63)/Rb(69)/Cs(79), Rb(63)/Cs(72)
X_{46}		
cage:	5^{12}	at [1/2,1/2,1/2]
cage:	$5^{12} 6^2$	at [1/2,0,1/4]
	cationic radii per cage	
C	0.449 0.680	Be(69), Li(88)/Mg(96)
Si	1.177 1.524	Na(81)/Ca(84)/Sr(96), Na(62)/Ca(65)/Sr(74)/K(87)/Ba(89)/Rb(97)
Ge	1.273 1.634	Na(75)/Ca(78)/Sr(89), Sr(69)/K(81)/Ba(83)/Rb(91)
Sn	1.735 2.148	Sr(65)/K(77)/Ba(78)/Rb(85)/Cs(97), K(62)/Ba(63)/Rb(69)/Cs(79)
X_{136}		
cage:	5^{12}	at [0,0,0]
cage:	$5^{12} 6^4$	at [3/8,3/8,3/8]
	cationic radii per cage	
C	0.449 0.875	
Si	1.179 1.828	
Ge	1.272 1.947	
Sn	1.737 2.512	
X_{172}		
cage:	5^{12}	at [0,0,0] and [0.75014,0.56576,1/2]
cage:	$5^{12} 6^2$	at [0.17815,*x*,0.24327] and [0.3732,0.9699,1/2]
cage:	$5^{12} 6^3$	at [0.89533,0.10467,1/2]
	cationic radii per cage	
C	0.492 0.441 0.690 0.686 0.786	
Si	1.156 1.169 1.536 1.530 1.682	
Ge	1.250 1.264 1.647 1.641 1.801	
Sn	1.707 1.721 2.148 2.142 2.320	

ratio of the radii of the cation and the cavity. Recent experimental results show that when a mixture of alkali and alkaline earth elements is used one can synthesize new structures.[24, 26, 27, 71, 72]

Representative structures chosen from our study are described below. The sodalite structure X_{12} (X = C, Si, Ge, Sn) is composed of both four- and six-membered rings. This ST has 12 framework atoms in its unit cell[73] which form fused truncated octahedra of 24 atoms (T_{24}). The notation m^i is used to denote the presence of *i* *m*-angular faces; thus, the building block of X_{12} can be expressed as $4^6 8^6$, since it has six square and six octagonal faces. X_{34} is a hexagonal structure seen in clathrate hydrates[74] which contains four-, five-, and six-membered rings that form a twenty-atom polyhedron with

twelve pentagonal faces (5^{12}, i.e., a dodecahedron). By addition of atoms to this polyhedron, other types of cages can be built, which differ in the number of hexagonal faces: T_{24} ($5^{12}6^2$), T_{26} ($5^{12}6^3$), and T_{28} ($5^{12}6^4$). X_{38} is seen in the amalgams A_3Hg_{20} (A = Rb, Cs)[75] and consists of three and four-membered rings. This ST differs from clathrate-I in the multiplicity of one of the framework atoms and leads to cages with an icosahedron (3^{20}) and a 20-atom polyhedron ($3^{12}4^86^2$). X_{40}, proposed as a structure of porous carbon,[76] contains only five- and six-membered rings. These rings generate three T_{20}, two T_{24}, and two T_{26} polyhedra per unit cell. X_{172} has similar types of cages to X_{40} and is observed for bromine hydrate.[77] In addition, we compare these phases to the framework of the known clathrate phases: X_{46} clathrate-I, which has two T_{20} and six T_{24} cages; X_{136} clathrate-II, which has sixteen T_{20} and eight T_{28}, both of which contain five- and six-membered rings; and the diamond structure X_8, which is a known form of elemental C, Si, Ge, and Sn. Finally, it is noted that these frameworks are in no way a comprehensive enumeration of all possible clathrate-type lattices, but they are sufficient for our current purposes to relate local structure to phase stability.

Table 4. Relative energies [eVatom^{-1}] of clathrate frameworks X_n at 4 e atom^{-1} from LDA and tight-binding (TB) approaches. See text for description of structures.

n	C	Si	Ge	Sn
LDA				
8	0.00	0.00	0.00	0.00
12	0.46	0.26	0.22	0.17
34	0.20	0.11	0.08	0.05
38	2.16	0.54	0.43	0.25
40	0.18	0.11	0.06	0.04
46	0.16	0.09	0.05	0.03
136	0.12	0.07	0.04	0.02
172	0.17	0.09	0.05	0.03
TB				
8	0.00	0.00	0.00	0.00
12	2.01	1.06	0.92	0.49
34	0.51	0.28	0.27	0.13
38	3.62	4.56	3.89	2.74
40	0.18	0.18	0.19	0.11
46	0.15	0.15	0.16	0.08
136	0.10	0.11	0.13	0.05
172	0.15	0.15	0.16	0.07

A useful measure of the stability of these phases is the relative energy of the undoped structures, as given in Table 4. The X_8 (diamond) structure is the lowest in energy for all elements. The next lowest in energy are the known phases X_{46} and X_{136}. What is most surprising is that X_{40} and X_{172} are only a few hundredths of an eV atom^{-1} higher in energy then these two phases. Most notably, Sn_{40}, Sn_{46}, Sn_{136}, and Sn_{172} are all isoenergetic within the accuracy of our calculations, and the situation for Ge is similar. The X_{34} phase is higher in energy than these phases, but much less so then either the X_{12} and X_{38} structures.

The tight-binding scheme predicts identical trends as the full DFT calculations, with the exception that the energy differences are larger, especially for the least stable phases. However, the tight-binding calculations are less computationally demanding and thus may serve as a quick method for screening phases. Another advantage of the tight-binding scheme is that the structures can be studied at any desired electron count to assess the dependence of energy on the number of valence electrons. For example, Figure 7 shows energy-difference curves for Ge_{12}, Ge_{38},and Ge_{40} phases relative to Ge_8. There is no qualitative difference between the curves for Ge_{40} and those of the remaining phases Ge_{46}, Ge_{136}, and Ge_{172}, and they are therefore omitted for clarity. Our analysis indicates that Ge_{12} is less stable than diamond at around 4 e atom^{-1} due largely to a fourth-moment effect, which results from the presence of the square faces. This framework is favorable above 5.5 e atom^{-1}, but it is unlikely that a suitable guest atom can be found which would donate such a large number of electrons. Thus, one would need to additionally substitute Group 15 elements into the framework to possibly obtain this species. The Ge_{38} structure is favored at low electron counts due to the large number of triangles (μ_3 effect) and thus unstable around 4 e atom^{-1}. Stabilization of this structure would require electronegative dopant atoms and/or Group 13 framework atoms. The Ge_{40} phase however, is stable above 4.2 e atom^{-1} due to the five-membered rings and, like the known phases, can be stabilized by doping. The same applies to Ge_{136}, Ge_{46}, and Ge_{172} which exhibit the same behavior as Ge_{40} largely due to the similarity in their

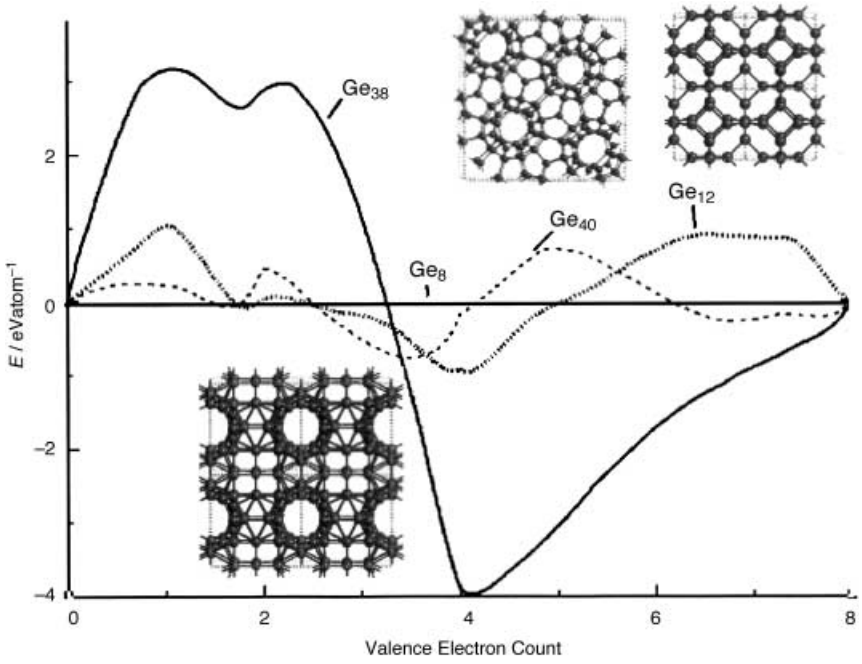

Figure 7. Energy-difference curves for the Ge_{12} (solid line), Ge_{38} (dashed line), and Ge_{40} (long dashed line) phases relative to the diamond structure. The convention for these plots is the same as in Figure 2.

  0947-6539/02/0812-2796 $ 20.00+.50/0 *Chem. Eur. J.* **2002**, *8*, No. 12

structures. The same trends are found for Sn, Si, and C as well. In general, structures with either four- or three-membered rings are not energetically compatible for electron counts around 4 e atom^{-1} as compared with structures consisting of five- and six-membered rings.

To understand why X_{40} and X_{172} have not been observed, with the notable exception of the recent report of Sn_{172},[72] even though their energies are comparable with those of known phases it is necessary to examine the size of the cages in these materials. Both frameworks consists of 20-, 24- and 26-membered polyhedra (see Table 3) into which electron-donating atoms can be intercalated. However, the disparity in size between these cages is large, and it would require either a ternary or quaternary composition to provide the ions that fit in the cages. For example, for Ge the 26-atom cage is large enough to accommodate Rb atoms, but the remaining two cages can only accommodate atoms no larger than K and Na. Since, to our knowledge, no such quaternary phases have been studied it is not surprising that these structures have not been observed. Moreover, our analysis suggests that it may indeed be possible to stabilize carbon-based clathrates by using Be and Li as dopants.

We now turn to the question of whether these materials are suitable for applications in thermoelectric devices. To investigate the thermal power of these phases we calculated the Seebeck coefficient S for fully optimized phases of $Na_3K_2Rb_2Si_{40}$, $Na_3K_2Cs_2Ge_{40}$, and Li_4C_{40}, all of which may result from the above doping scheme. Similar to the known clathrate phases at high doping levels, these compounds are calculated to have low values of S at 300 K of about 5 – 10 μV K^{-1} and thus would not be useful thermoelectrics.[9, 40, 44, 45] As in our previous study[9] it was found that an estimate of S for variable concentrations can be obtained by assuming a rigid-band model (derived from the empty cage) and monitoring S as a function of increasing Fermi energy. This is done by filling the empty orbitals of the vacant lattice with ε electrons, which artificially increases the Fermi level, and recalculating S. This function is plotted for three such hypothetical band fillings for the Si_{40} lattice in Figure 8. The thermal power is almost 25 times higher than that of the fully loaded structure at 300 K for the lowest doping level ($\varepsilon = 0.03$ e per Si_{40} unit) and falls off rapidly to only a factor of 10 for $\varepsilon = 0.5$ e per Si_{40}. In practice, this would require extremely low doping levels, which identical to the situation found for the phases based on Si_{46}.[9] Similar findings were made for the Ge_{40} and C_{40} phases.

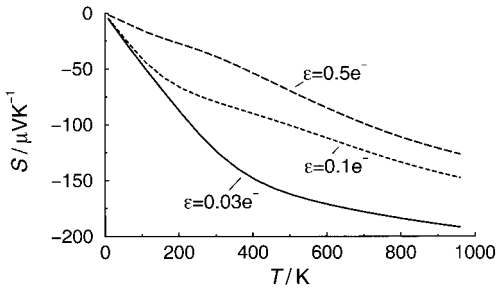

Figure 8. Seebeck coefficient S as a function of temperature for Si_{40}. Values were obtained by using a rigid-band model with a Fermi level determined by increasing the valence electron count by ε electrons.

Thus, the X_{172} and X_{40} structures are likely candidates for stable phases if they are synthesized with a combination of large and small alkali metal cations. However, like X_{136} and X_{46} the thermal power of these phases is low at maximum doping; hence removal of alkali metal atoms after formation would be required to maximize this property.

Conclusion

In summary, we have demonstrated a systematic way to understand the evolution of the crystal structures of intermetallic and alloy phases in real space. Fundamental to this approach is the realization that the metallic bond can be thought of as a specific class of covalent bonding which is not saturated by two electrons. Most importantly, there is a practical benefit to this approach. One can sift through various geometrical possibilities for a given stoichiometry and perform a low-level calculation to aid in selecting low-energy structures on the basis of local geometrical features. These phases can then be modeled by first-principles calculations to obtain high-quality numerical data for thermodynamic and transport properties. Future investigations will center on extending the theory to account for pressure effects and on correlating elastic properties to local structural motifs.

Acknowledgement

We are grateful to Svilen Bobev, Micheal Ferguson, Dennis Klug, Stephen Lee, Chris Ratcliffe, and Slavi Sevov for insightful discussions.

[1] J. K. Burdett, *Chemical Bonding in Solids.* Oxford, New York, **1995**.
[2] D. Pettifor, *Bonding and Structure of Molecules and Solids*, Clarendon Press, Oxford, **1995**.
[3] R. O. Jones, O. Gunnarsson, *Rev. Mod. Phys.* **1989**, *61*, 689.
[4] V. Heine in *Solid State Physics*, *Vol. 35* (Eds.: H. Ehrenreich, F. Seitz, D. Turnbull), Academic Press, New York, **1980**.
[5] J. K. Burdett, S. Lee, W. C. Sha, *Crot. Chem.* **1984**, *57*, 1193.
[6] J. K. Burdett, S. Lee, *J. Am. Chem. Soc.* **1985**, *107*, 3050; *J. Am. Chem. Soc.* **1985**, *107*, 3063.
[7] S. Lee, *Acc. Chem. Res.* **1991**, *24*, 249.
[8] S. Lee, *Ann. Rev. Phys. Chem.* **1996**, *47*, 397.
[9] J. S. Tse, K. Uehara, R. Rousseau, A. Ker, C. I. Ratcliffe, M. A. White, G. Mackay, *Phys. Rev. Lett.* **2000**, *85*, 114; *Phys. Rev. Lett.* **2001**, *86*, 4980.
[10] R. Rousseau, J. S. Tse, *Prog. Theor. Phys. Supp.* **2000**, *138*, 47.
[11] R. Rousseau, E. Todorov, K. Uehara, J. S. Tse, *Technical Proceedings of International Conference on Computational Nanoscience*, **2001** 125.
[12] J. S. Tse, K. Ueharar, Z.-Q. Li, R. Rousseau, D. D. Klug, *Electronic Mater.*, in press
[13] S. Lee, *J. Am. Chem. Soc.* **1991**, *113*, 101.
[14] L. M. Hoistad, *Inorg. Chem.* **1995**, *34*, 2711.
[15] U. Häussermann, M. Wörle, R. Nesper, *J. Am. Chem. Soc.* **1996**, *118*, 11789.
[16] U. Häussermann, R. Nesper, *J. Alloys and Comp.* **1995**, *118*, 244.
[17] R. Podloucky, H. J. F. Jansen, X.-Q. Guo, A. J. Freeman, *Phys. Rev. B* **1988**, *35*, 15478.
[18] X.-Q. Guo, R. Podloucky, A. J. Freeman, *Phys. Rev. B* **1989**, *40*, 2793.
[19] K. Masuda-Jindo, K. Terakura, *Phys. Rev. B* **1989**, *39*, 7590.
[20] X.-Q. Guo, R. Podloucky, A. J. Freeman, *Phys. Rev. B* **1990**, *42*, 10912.
[21] X.-Q. Guo, R. Podloucky, J. Xu, A. J. Freeman, *Phys. Rev. B* **1990**, *41*, 12432.

  0947-6539/02/0812-2797 $ 20.00+.50/0

[22] J. S. Kasper, P. Hagenmuller, M. Pouchard, C. Cros, *Science* **1965**, *150*, 1713.
[23] B. Eisenmann, H. Schäfer, R. Zagler, *J. Less-Comm. Metals* **1986**, *118*, 43.
[24] S. Bobev, S. C. Sevov, *J. Am. Chem. Soc.* **1999**, *121*, 3795.
[25] E. Reny, S. Yamanaka, M. Puchard, *Chem. Commun.* **2000**, 2505.
[26] S. Bobev, S. C. Sevov, *Inorg. Chem.* **2000**, *39*, 5930.
[27] S. Bobev, S. C. Sevov, *J. Solid State Chem.* **2000**, *151*, 92.
[28] W. Carrillo-Cabrera, J. Curda, H. G. von Schnering, S. Paschen, Y. Grin, *Z. Krist.* **2000**, *215*, 207.
[29] W. Carrillo-Cabrera, J. Curda, K. Peters, S. Paschen, Y. Grin, H. G. von Schnering *Z. Krist.* **2001**, *216*, 183.
[30] H. Kawaji, H. Hori, S. Yamanaka, M. Ishikawa, *Phys. Rev. Lett.* **1995**, *74*, 1427.
[31] G. B. Adams, M. O'Keffe, A. A. Demkov, O. F. Sankey, Y.-M. Huang, *Phys. Rev. B* **1994**, *49*, 8084.
[32] S. Saito, A. Oshiyama, *Phys. Rev. B* **1995**, *51*, 2628.
[33] E. Galvani, G. Onida, S. Serra, G. Benedik, *Phys. Rev. Lett.* **1996**, *77*, 3573.
[34] V. Smelyansky, J. S. Tse, *Chem. Phys. Lett.* **1997**, *264*, 459.
[35] M. O'Keffe, G. B. Adams, O. F. Sankey, *Phil. Mag. Lett.* **1998**, *78*, 21.
[36] J. Zhao, A. Buldum, J. P. Lu, C. Y. Fong, *Phys. Rev. B* **1999**, *60*, 14177.
[37] J. Dong, O. F. Sankey, *J. Phys. Cond. Mater.* **1999**, *11*, 6129.
[38] C. A. Perottoni, J. A. H. de Jornada, *J. Phys. Condens. Mater.* **2001**, *13*, 5981.
[39] R. Nesper, K. Vogel, P. E. Blóchl, *Angew. Chem.* **1993**, *105*, 786; *Angew Chem. Int. Ed. Eng.* **1993**, *32*, 701.
[40] G. S. Noles, J. L. Cohn, G. A. Slack, S. B. Schujman, *Appl. Phys. Lett.* **1998**, *73*, 178.
[41] Y. Guyot, L. Grosvalet, B. Champagnon, S. Reny, C. Cros, M. Pouchard, *Phys. Rev. B* **1999**, *60*, 14507.
[42] T. Kawaguchi, K. Tanigaki, M. Yasukawa, *Phys. Rev. Lett.* **2000**, *85*, 3189.
[43] G. S. Noles, T. J. R Weakley, J. L. Cohn, R. Sharma *Phys. Rev. B* **2000**, *61*. 3845.
[44] L. Qui, M. A. White, Z. Li, J. S. Tse, C. Ratcliffe, C. A. Tulk, J. Dong, O. Sankey, *Phys. Rev. B* **2001**, *64*, 24303.
[45] J. S. Tse, Z. Li, K. Uehara, *Eur. Phys. Lett.* **2001**, *56*, 261.
[46] S. Lee, *J. Am. Chem. Soc.* **1991**, *113*, 101.
[47] D. G. Pettifor, R. Podlucky, *Phys. Rev. Lett.* **1984**, *53*, 1080.
[48] R. Rousseau, S. Lee, *J. Chem. Phys.* **1994**, *101*, 10753.
[49] E. Todorov, M. Evans, S. Lee, R. Rousseau, *Chem. Eur. J.* **2001**, *7*, 2652.
[50] S. Lee, B. Foran, *J. Am. Chem. Soc.* **1994**, *116*, 154.
[51] G. B. Bachelet, D. R. Hamann, M. Schluter, *Phys. Rev. B* **1982**, *26*, 4199.
[52] As our starting point we use the parameter set compiled by Edgar Muller (Edgar.Muller@icma.unil.ch).
[53] P. Turchi, F. Ducastella, G. Trégoa, *J. Phys. C Solid State Phys.* **1982**, *37*, 2891.
[54] G. Allan, *J. Phys. C Solid State Phys.* **1984**, *38*, 3945.
[55] D. Vanderbilt, *Phys. Rev. B* **1990**, *41*, 7892.
[56] H. J. Monkhorst, J. F. Pack, *Phys. Rev. B* **1976**, *13*, 5188.
[57] J. P. Perdew, Y. Wang, *Phys. Rev. B* **1991**, *45*, 13244.
[58] G. Kresse, J. Hafner, *Phys. Rev. B* **1993**, *47*, 55; *Phys. Rev. B* **1994**, *49*, 14251.
[59] G. Kresse, J. Furthmüller, *Comput. Mater. Sci.* **1995**, *6*, 15.
[60] G. Kresse, J. Furthmüller, *Phys. Rev. B* **1996**, *54*, 11169.
[61] J. M. Ziman, *Principles of the Theory of Solids* University Press, Cambridge **1972**.
[62] K. Uehara, T. S. Tse, *Phys. Rev. B* **2000**, *61*, 1639.
[63] D. D. Koelling, J. H. Wood, *J. Comput. Phys.* **1986**. *67*, 253.
[64] W. E. Pickett, H. Krakauer, P. B. Allen, *Phys. Rev. B* **1988**, *38*, 2721.
[65] P. Blaha, K. Schwarz, J. Luitz, WIEN97, A Full Potential Linearized Augmented Plane Wave Package for Calculating Crystal Properties, Karlheinz Schwarz, Techn. Univ. Wien, Vienna **1999**.
[66] J. D. Corbett, *Angew. Chem.* **2000**, *112*, 682; *Angew. Chem. Int. Ed. Eng.* **2000**, *39*, 670.
[67] *Alloy Phase Diagrams. Vol. 3* (Ed.: H. Baker), ASM International, Materials Park, OH, **1992**.
[68] S. Lee, R. Rousseau, C. Wells, *Phys. Rev. B* **1992**, *46*, 12121.
[69] The GGA calculated structures: Li_5Al_4 (space group $P\bar{3}m1$) Li 1b(0,0,1/2), 2d(1/3,2/3,0.619) and 2d(1/3,2/3,0.947); Al 2c(0,0,0.831) and 2d(1/3,2/3,0.279). Li_2Al_3 (space group $P4/m$) Li 4k(0.109,0.701,1/2); Al 1a(0,0,0), 1d(1/2,1/2,1/2) and 4j(0.401,0.802,0). Lattice constants are given in Table 1.
[70] The search was conducted over the structure types as obtained from P. Villars, L. D. Calver, *Pearson's Handbook of Crystallographic Data of Intermetallic Phases*, ASM, Metals Park, OH, **1985**. The numbers in parentheses are the relative energies in electron volts obtained from gradient-corrected DFT calculations. The phases are: Al_3Pt_2 (0.74), Al_2Zr_3 (0.72), Cu_3Ti_2 (0.33), Ga_3Ti_2 (0), La_2Ni_3 (0.65), Ni_3Sn_2 (0.42), Pd_3Te_2 (0.59), Pd_3Ti_2 (0.08), Pt_2Sn_3 (0.55), Pt_3Tl_2 (0.23), Ru_2Si_3 (0.43).
[71] S. Bobev, S. Sevov, personal communication
[72] S. Bobev, S. C. Sevov, *J. Am. Chem. Soc.* **2001**, *123*}, 3389.
[73] L. Pauling, *Z. Krist.* **1930**, *74*, 213.
[74] K. A. Udachin, G. D. Enright, C. I. Ratcliffe, J. A. Ripmester, *Supramol. Chem.* **1997**, 8, 173.
[75] E. Todorov, S. C. Sevov, *J. Solid State Chem.* **2000**, *149*, 419.
[76] G. Benedek, E. Galvani, S. Sanguinetti, S. Serra, *Chem. Phys. Lett.* **1995**, *244*, 339.
[77] K. A Udachin, G. D. Enright, C. I. Ratcliffe, J. A. Ripmester, *J. Am. Chem. Soc.* **1997**, *119*, 11481.

Received: October 29, 2001
Revised: March 5, 2002 [F3638]

  0947-6539/02/0812-2798 $ 20.00+.50/0